The range and nature of effective interactions in hard-sphere solids

Michael Schindler[*a] and A. C. Maggs[a]

Colloidal, hard sphere materials are often modeled by short-ranged, pairwise repulsive interactions. We study the matrix of correlations of particle displacements, which has often been studied experimentally. The inverse of this matrix can be interpreted as an effective dynamical matrix. We study the range and nature of the effective interactions that are generated in this mapping, and we characterise the interactions which give rise to violations of the Cauchy relations in elasticity.

1 Introduction

Many experimental groups are now performing high statistics imaging of colloidal materials with the aim of extracting the displacement–displacement correlation function between many particles. The question for the theorist is then how to describe the link between the matrix of correlations and macroscopic properties of the material. The microscopic interactions between colloids can be very different, depending on the detailed chemistry of the materials. For instance, both deformable[1] and hard particles[2] are available for the experimentalist to study. This paper treats in detail the case of hard-sphere crystals where elasticity is generated from entropy changes.

Once the matrix of correlations between particle displacements, G, is available, it is traditional to invert it[3–9] and to interpret the result as the effective "dynamical matrix" D for the particles[10] – one can also extract the elastic moduli, characteristic of the underlying solid. However, there are surprises and subtleties in the results. In particular the effective interactions in the hard-sphere system turn out to show substantial deviations from the Cauchy relation for elastic solids.[11–14] The Cauchy relations reduce the number of independent elastic constants in materials below the number expected from counting arguments and symmetry. Cauchy found that linear relations occur between *a priori* independent constants if a particular microscopic constitutive relation is assumed; the Cauchy relations apply if interactions between atoms (or colloids) are pairwise, central and sufficiently short ranged. The Cauchy relations can be written as an equality $\lambda = \mu$ between two Lamé coefficients in the cases of a two-dimensional hexagonal crystal or a cubic crystal in three dimensions. For the latter one finds in Voigt notation $C_{12} = C_{44}$. The breakdown of Cauchy's relation in hard-sphere crystals (with short-ranged central interactions) is thus a *small* surprise, though as showed by

Hoover[15] extra contributions (beyond those found by Born[10]) are found in the expressions for the elastic constants at any finite temperature.

In this paper we characterise the effective "spring constants" (that is elements of the matrix D) between particles in a colloidal crystal in one, two and in three dimensions. We show that beyond one dimension effective interactions extend beyond first nearest neighbour in the crystal. We also examine the nature of contributions to the dynamical matrix which do not occur in "Cauchy" materials, defined here as materials with rapidly decaying central interactions.

2 Numerical results

We performed *very high statistics* event-driven molecular dynamics simulations of N hard spheres in one, two and three dimensions ($d = 1, 2, 3$). In one dimension the particles are confined to a line. In two dimensions we simulate a hexagonal crystal within a box adapted to the Bravais lattice. In three dimensions we perform simulations of face-centred cubic crystals, again within a box adapted to the Bravais lattice. In all dimensions the simulation box is continued periodically. During a simulation the total momentum and the (kinetic) energy are conserved. The densities are always so high that no particle interchange occurs over the simulation time, so that particle diffusion and defects can be neglected in the data analysis. The Bravais lattice thus defines the reference positions of the spheres, and these coincide with the average positions.

For all numerical data the units are chosen such that the particles have unit diameter, unit mass, and that $kT = 1$ with T the temperature. Throughout the paper, Greek indices denote spatial directions, and $\mathbf{i}, \mathbf{j}, \mathbf{m}, \mathbf{n}$ are tuples of integer indices on the Bravais lattice. They identify the sites on the lattice. The spatial (Euclidean) positions of lattice sites are denoted by vectors, $\mathbf{R_i}$ for lattice site $\mathbf{i}$. The $\mathbf{R_i}$ are multiples of the lattice spacing d_0. All differences between lattice indices, $\mathbf{i} - \mathbf{j}$, or lattice positions,

[a] UMR Gulliver 7083 CNRS, ESPCI ParisTech, PSL Research University, 10 rue Vauquelin, 75005 Paris, France

$\mathbf{R_{i-j}} = \mathbf{R_i} - \mathbf{R_j}$ are understood *modulo the periodicity*, the result being mapped back into a centered copy of the simulation box.

During the simulation we take a series of K data recordings. For each recording, we measure the deviations $\mathbf{u_i} := \mathbf{r_i} - \mathbf{R_i}$ of the instantaneous particle positions from their reference positions and calculate the $dN \times dN$ correlation matrix

$$G_{(\mathbf{i},\alpha)(\mathbf{j},\beta)} := \frac{1}{K} \sum_{k=1}^{K} u_{\mathbf{i}\alpha} u_{\mathbf{j}\beta} \tag{1}$$

The matrix has a simple physical interpretation from linear response theory: It determines the vectorial displacement at $\mathbf{j}$ due to a force at $\mathbf{i}$. We will thus call it a Green function in the following. In order to reduce statistical noise, we average elements of G which are related by the translational symmetry of the lattice,

$$G_{\alpha\beta}(\mathbf{n}) := \frac{1}{N} \sum_{\mathbf{i}} G_{(\mathbf{i},\alpha)(\mathbf{i}+\mathbf{n},\beta)}. \tag{2}$$

The sum runs over all sites of the Bravais lattice. We could also have averaged over the rotational and inversion symmetries, but we preferred to see the symmetries appear from the data in order get a idea of the statistical errors; the translational average appeared to be sufficient for noise reduction. A visual representation of the elements of $G(\mathbf{n})$ in two dimensions is given in Fig. 1. It is a rather structureless object, and it depends on the size and shape of the periodic box due to the logarithmic nature of two-dimensional Green functions. In the figure we plot the elements of $G(\mathbf{n})$ in a rotated coordinate system with one basis vector aligned with the vector $\mathbf{R_n}$. We note in particular the interesting physical structure that occurs in the off-diagonal elements. These elements of the response function vanish along high symmetry directions: a force along these symmetry directions gives a purely parallel displacement. This gives rise to a set of radial white lines in the lowest panel of Fig. 1.

We then use matrix algebra to numerically invert the large matrix G to produce the effective interaction matrix D. More precisely, we use the translation-averaged $dN \times dN$ matrix

$$G_{\alpha\beta}(\mathbf{i},\mathbf{j}) := G_{\alpha\beta}(\mathbf{j}-\mathbf{i}). \tag{3}$$

and take its Moore–Penrose pseudoinverse because we must avoid inversion of the zero eigenvalues in G which come from momentum conservation. The inverse is denoted by $D_{\alpha\beta}(\mathbf{i},\mathbf{j})$. In the following, we will analyse the properties of the resulting 2×2 matrices

$$D_{\alpha\beta}(\mathbf{n}) := \frac{1}{N} \sum_{\mathbf{i}} D_{\alpha\beta}(\mathbf{i},\mathbf{i}+\mathbf{n}). \tag{4}$$

We note that in a linear network all correlations can be calculated from G via Wick's theorem. If one builds a network with linear springs and short-ranged interactions, it is natural that $D(\mathbf{n})$ is sparse, i.e. that it is *exactly* zero for most $\mathbf{n}$. One of the questions that we answer in this paper is to what degree this remains true for the effective interactions generated in hard-sphere materials.
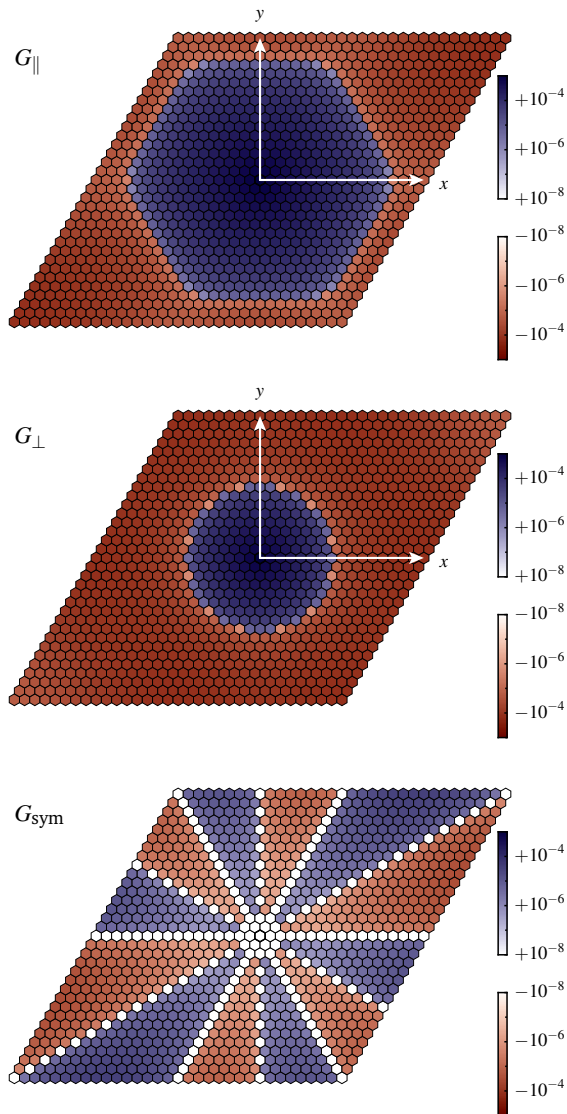
Fig. 1 The two-dimensional Green function in a periodic 32×32 hexagonal lattice. Plotted are the components of the 2×2 matrices $G_{\alpha\beta}(\mathbf{n})$ in a rotated orthonormal basis $(\hat{\mathbf{R}}_\mathbf{n}, \hat{\mathbf{o}})$: $G_{\parallel} = \hat{\mathbf{R}}_\mathbf{n}^T G \hat{\mathbf{R}}_\mathbf{n}$, $G_{\perp} = \hat{\mathbf{o}}^T G \hat{\mathbf{o}}$, $G_{\text{sym}} = (\hat{\mathbf{R}}_\mathbf{n}^T G \hat{\mathbf{o}} + \hat{\mathbf{o}}^T G \hat{\mathbf{R}}_\mathbf{n})/2$. The antisymmetric off-diagonal terms vanish to within statistical noise ($\pm 10^{-9}$). In the lowest panel the white lines correspond to a mechanical response parallel to an imposed force.
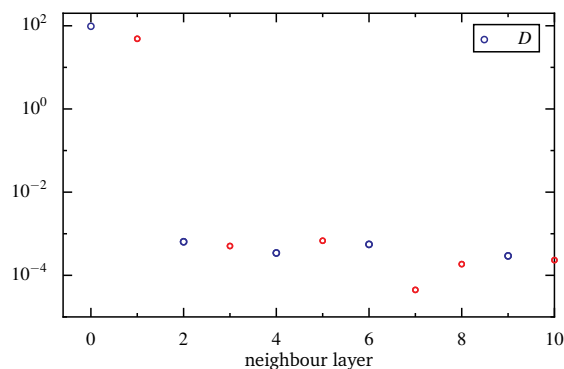
Fig. 2 The effective interactions $D(j - i)$ in a one-dimensional chain of $N = 100$ impenetrable rods. Larger blue symbols are positive values, smaller red are symbols negative values. $K \sim 10^7 N$ recordings. Beyond nearest neighbours the interactions are zero to within statistical noise.

2.1 One-dimensional system

Previous work has led to a detailed understanding of the one-dimensional problem.[16] We do not treat it in detail, but rather use it to check some of the chain of data analysis. The result is very simple – that the effective interaction in one dimensional fluids is limited to nearest neighbours; for larger separations D is zero. We used our code for simulation and data analysis and confirmed this results. Beyond the nearest neighbour, the effective interaction $D(j - i)$ in Fig. 2 falls to zero within statistical noise. Note that the relative statistical noise in this plot is at the level of 10^{-5}, showing the *very high precision* simulations with very large data sets. Given the excellent results found in one dimension, we can feel confident that the very different results found in two and in three dimensions are a result of differing physics, and not problems related to systematic or statistical errors in the data sets.

In the data of Fig. 2 we find the ratio between the two nonzero values to be $D(0)/D(1) = -2.0 \pm 10^{-5}$. This is precisely the ratio that is expected from a discretisation of the Laplacian operator in terms of nearest neighbours. We thus found the expected result, namely that the inverse of the (static) Green function is the corresponding differential operator of one-dimensional (static) elasticity.

2.2 Two-dimensional crystal

We started by performing simulations in systems with $N = L \times L$ hard disks, L varying from 10 to 100 with fixed surface fraction $\phi = 0.85$. We expect that the elements of the effective dynamical matrix D come from the local physics (and available entropy) occurring near each particle and are not the results of a non-trivial propagation of boundary effects down to the microscopic scale. If the physics is local we then expect that the values of the elements of D vary very little with changes in the system size. To test this we plot in Fig. 3 the evolution of $\text{tr}(D)$ with the system size L and find that the lines involving the evolution of D for small separations are remarkably stable. This is true for all matrix elements of $D_{\alpha\beta}$, not only for the trace. Since we are performing simulations within a periodic box, it is clear that we should only be evaluating elements for separations such that periodic copies do not contaminate the result. Thus we will only quantitatively analyse D for
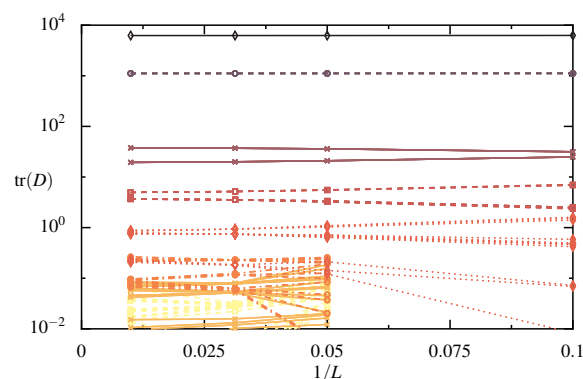
Fig. 3 Effective interactions as a function of the inverse system size $1/L$. Different plot styles correspond to different neighbour layers, starting from 0 at the top, down to 7. Fewer layers are plotted for $L = 10$.
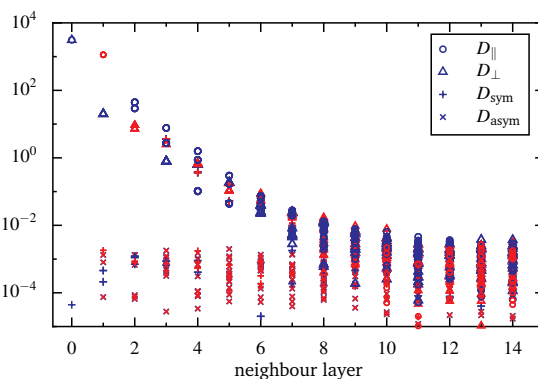
Fig. 4 Effective interactions in a hexagonal hard-disk crystal with $L = 32$. Larger blue symbols are positive values, smaller red symbols are negative values. $K \sim 3.5 \times 10^6 \, 2N$ recordings. Surface fraction $\phi = 0.85$. These data required around 300 000 CPU core hours.

separations which are smaller than $L/2$.

The correlation function G, which is measured in the simulations and displayed in Fig. 1, is subject to strong finite size corrections due to the logarithmic nature of two-dimensional Green functions. The components of the matrix D, however, do not evolve for small values of $1/L$. From the curves in Fig. 3 we decided to use a fixed value of $L = 32$ for further simulation in order to collect the highest possible statistics, while being able to resolve effective interactions out to a large distance.

The resulting matrix elements are plotted in Fig. 4. As we did already in Fig. 1, we rotated the 2×2 matrices $D_{\alpha\beta}(\mathbf{n})$ for each separation vector $\mathbf{R_n}$. Using the orthonormal rotated basis $(\hat{\mathbf{R}}_{\mathbf{n}}, \hat{\mathbf{o}})$, where the hat denotes a normalised vector, the interactions plotted in Fig. 4 are

$$D_{\parallel}(\mathbf{n}) := \hat{\mathbf{R}}_{\mathbf{n}}^T D(\mathbf{n}) \hat{\mathbf{R}}_{\mathbf{n}}$$

$$D_{\perp}(\mathbf{n}) := \hat{\mathbf{o}}^T D(\mathbf{n}) \hat{\mathbf{o}}$$

$$D_{\text{sym}}(\mathbf{n}) := \left(\hat{\mathbf{R}}_{\mathbf{n}}^T D(\mathbf{n}) \hat{\mathbf{o}} + \hat{\mathbf{o}}^T D(\mathbf{n}) \hat{\mathbf{R}}_{\mathbf{n}} \right)/2 \quad (5)$$

$$D_{\text{asym}}(\mathbf{n}) := \left(\hat{\mathbf{R}}_{\mathbf{n}}^T D(\mathbf{n}) \hat{\mathbf{o}} - \hat{\mathbf{o}}^T D(\mathbf{n}) \hat{\mathbf{R}}_{\mathbf{n}} \right)/2.$$

The interaction in Fig. 4 does *not* vanish beyond the first layer
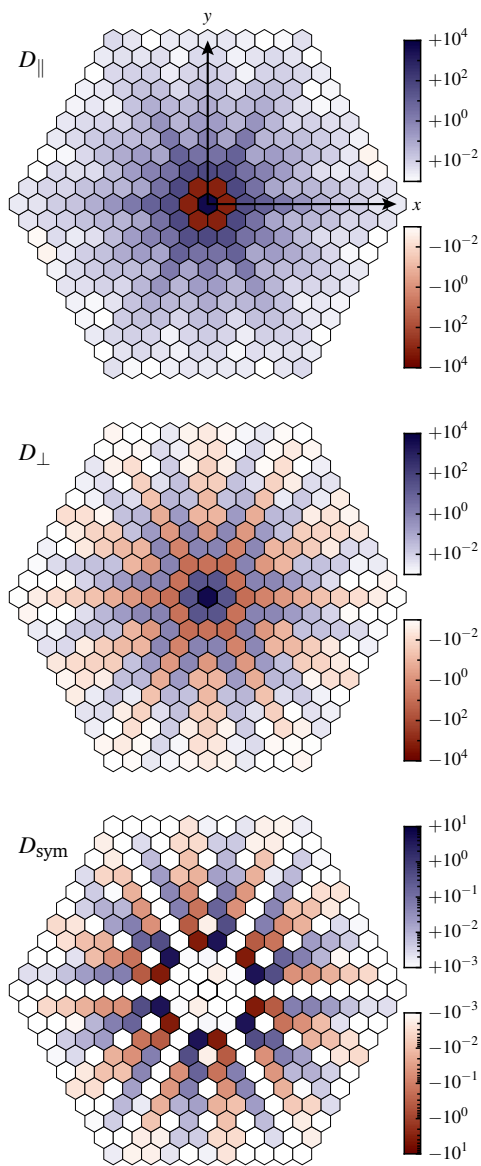
Fig. 5 Matrix elements of $D(\mathbf{n})$ in rotated frames of reference, for several $\mathbf{R_n}$. The center of the hexagon corresponds to $\mathbf{R_n} = \mathbf{0}$. The antisymmetric off-diagonal D_{asym} vanishes to within statistical noise. The reflection anti-symmetry of D_{sym} imposes that the elements of D_{sym} are zero for the first two neighbour layers. All elements of D_{sym} are small compared to $D_{\parallel}$ and $D_{\perp}$.
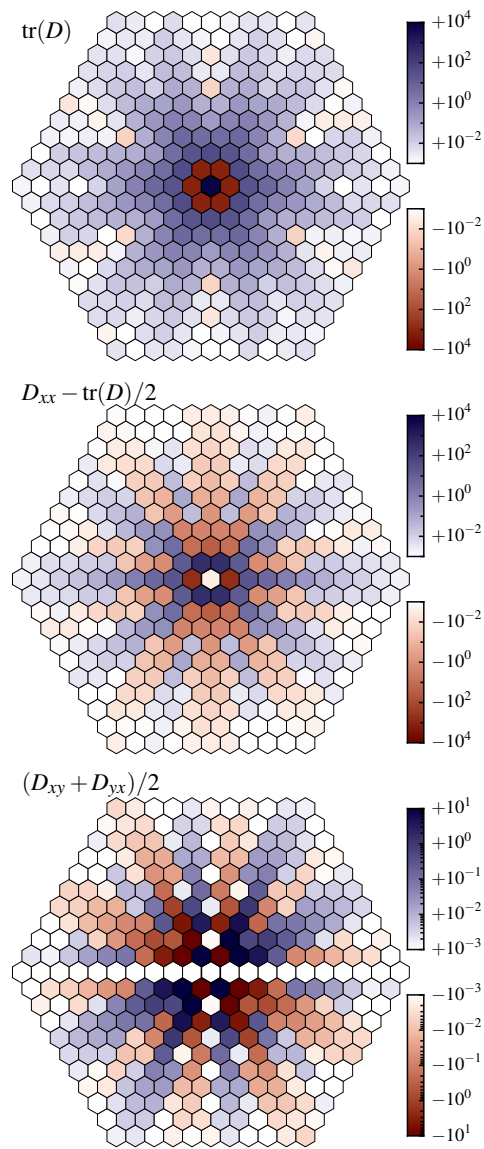
Fig. 6 Some linear combinations of matrix elements $D_{\alpha\beta}(\mathbf{n})$ for several $\mathbf{R_n}$. The antisymmetric off-diagonal $(D_{xy} - D_{yx})/2$ vanishes to within statistical noise.

of neighbours – very differently from its unidimensional counterpart in Fig. 2. We here observe that $D(\mathbf{n})$ is not sparse. We used high statistics in this plot to be sure that the interaction data is well separated from statistical noise. We find it to be the case for the first six layers of neighbours. The noise level can be read off from the values of D_{asym} which are zero in noiseless data. Another measure of the statistical noise is the spread of those symbols which are equal by symmetry of the lattice.

We tried to characterise the decay of the effective interactions with particle separation, which we can resolve out to the eighth layer of neighbours. We tried fitting the data with both exponential and power law decays, plotting both particle separation and layer number for the abcissa. No fit seemed totally convincing with our data. If one insists on fitting with a power law $\|\mathbf{R_n}\|^{\alpha}$, one finds $\alpha \approx -6 \pm 0.5$. At the moment we do not have analytic arguments that predict the functional form of the decay.

2.2.1 Two-dimensional visualisation

We now give some more details of the data presented in Fig. 4. In particular, we like to visualise those points which are characterised by being within same neighbour level, but which differ with respect to the hexagonal symmetry.

We can study the 2×2 matrices $D(\mathbf{n})$ in different frames of reference. The first frame of reference is the orthonormal basis $(\hat{\mathbf{R}}_\mathbf{n}, \hat{\mathbf{o}})$ already used above. In Fig. 5 we plot the parallel, the orthogonal, and the off-diagonal component of the matrix. All three panels are invariant under rotations of 60 degrees. Under mirroring, however, only the first two are invariant while D_{sym} changes sign. We did not plot D_{asym} because it contains only noise.

A second manner of examining the data is in the fixed Cartesian frame, which is the same for all $\mathbf{n}$. In Fig. 6 we study the trace of the matrix, $\mathrm{tr}(D)$, the first component D_{xx} of which we subtracted half the trace, and the off-diagonal element D_{xy}, symmetrised. The component $D_{yy} - \mathrm{tr}(D)/2$ is not plotted as it is simply the negative of $D_{xx} - \mathrm{tr}(D)/2$. Only $\mathrm{tr}(D)$ still has hexagonal symmetry. The two bottom panels show (skew) symmetry with respect to mirroring about the x-axis and the y-axis. The special choice of component combinations in Fig. 6 is motivated by the continuum limit which we discuss now.

2.2.2 Hexagonal continuum limit

The matrix $D_{\alpha\beta}(\mathbf{n})$ is the inverse of the Green function of static elasticity and is thus expected to be related to the corresponding differential operator – or rather its hexagonal discretisation. We now summarize the usual continuum elastic theory to establish the expectation for D if the elastic tensor were a simple constant. Starting with the elastic constant for a hexagonal crystal in two dimensions in terms of Lamé coefficients,

$$C_{\alpha\beta\sigma\tau} = \lambda \delta_{\alpha\beta}\delta_{\sigma\tau} + \mu \left(\delta_{\alpha\sigma}\delta_{\beta\tau} + \delta_{\alpha\tau}\delta_{\beta\sigma} \right), \tag{6}$$

we find the differential operator to be (Sec. 3 of Ref. 13)

$$\mathscr{D}_{\alpha\sigma} = -A_{\alpha\beta\sigma\tau}\partial_\beta\partial_\tau, \quad \text{with} \tag{7}$$

$$A_{\alpha\beta\sigma\tau} := C_{\alpha\beta\sigma\tau} + T_{\beta\tau}\delta_{\alpha\sigma}. \tag{8}$$

The two elastic tensors A and C coincide for systems whose reference state is stress-free. The hard-sphere crystal in our numerical simulation is compressed by the periodic boundary conditions, leading to the isotropic stress $T_{\beta\tau} = -P\delta_{\beta\tau}$ with the pressure P. Consequently, the two tensors A and C are different. Assembling these results, we find

$$\mathscr{D}_{\alpha\beta} = -(\mu - P)\delta_{\alpha\beta}\nabla^2 - (\lambda + \mu)\partial_\alpha\partial_\beta. \tag{9}$$

For these second derivatives, we can produce simple discretisations in terms of finite differences on nearest neighbours. In particular, the combinations of matrix elements used in Fig. 6 are simple combinations of second derivatives,

$$\mathrm{tr}\,\mathscr{D} \propto -\nabla^2 = \frac{1}{3d_0^2} \begin{array}{ccc} -1 & & -1 \\ -1 & +6 & -1 \\ -1 & & -1 \end{array} \tag{10}$$

$$\mathscr{D}_{xx} - \frac{\mathrm{tr}\,\mathscr{D}}{2} \propto \partial_y^2 - \partial_x^2 = \frac{1}{3d_0^2} \begin{array}{ccc} +1 & & +1 \\ -2 & 0 & -2 \\ +1 & & +1 \end{array} \tag{11}$$

$$\frac{\mathscr{D}_{xy} + \mathscr{D}_{yx}}{2} \propto -\frac{\partial_x\partial_y + \partial_y\partial_x}{2} = \frac{1}{\sqrt{3}d_0^2} \begin{array}{ccc} +1 & & -1 \\ 0 & 0 & 0 \\ -1 & & +1 \end{array} \tag{12}$$

We see that these stencils are qualitatively reproduced in the central parts of the panels in Fig. 6. However, Fig. 6 shows nonzero interactions also beyond the first layer of neighbours. Another difference is that for $\mathrm{tr}(D)$ we find a middle value which is -5.6 times the values found on the first neighbours (instead of -6). When comparing the values of the first neighbours among themselves, the stencils are again well reproduced, with variations as small as $\sim 10^{-5}$ in all three panels of Fig. 6. The skew symmetry of the operator $\partial_x\partial_y$ is found again in all values of $D_{xy}(\mathbf{n})$. This symmetry imposes the horizontal and the vertical white lines (zeros) in the third panel of Fig. 6.

The matrix $D_{\alpha\beta}(\mathbf{n})$ encodes the full dispersion curves that are required to determine the spectral properties of the fluctuations. In particular, one can extract the elastic tensor A from the long-wavelength limit. The usual way to do this calculation is to perform a discrete periodic (fast) Fourier transform on the matrix $G_{\alpha\beta}(\mathbf{i}, \mathbf{j})$ and to observe that the translation invariance renders the result block-diagonal. For each reciprocal vector $\mathbf{Q_m}$ we have one Fourier transformed $d \times d$ matrix
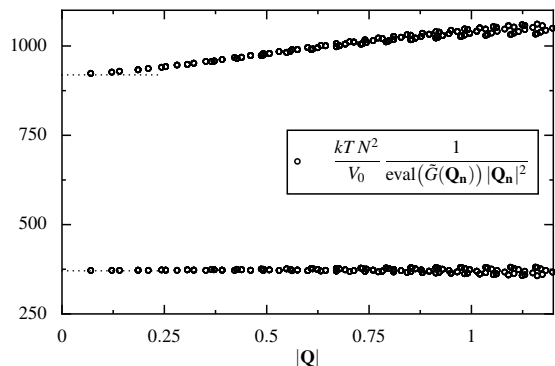
$$\tilde{G}_{\alpha\beta}(\mathbf{m}) := N \sum_{\mathbf{n}} e^{-i\mathbf{Q_m}\cdot\mathbf{R_n}} G_{\alpha\beta}(\mathbf{n}) \tag{13}$$

$$= \left\langle \overline{\tilde{u}_\alpha(\mathbf{m})}\tilde{u}_\beta(\mathbf{m}) \right\rangle. \tag{14}$$

The overline denotes a complex conjugate. To leading order, this matrix scales as $|\mathbf{Q_m}|^{-2}$, such that we can extract the elastic tensor as the long-wavelength prefactor to this scaling,

$$A_{\alpha\sigma\beta\tau}\hat{Q}_\sigma\hat{Q}_\tau = \frac{kT\,N^2}{V_0} \lim_{|\mathbf{Q_m}|\to 0} \frac{\left[\tilde{G}(\mathbf{m})^{-1}\right]_{\alpha\beta}}{|\mathbf{Q_m}|^2}. \tag{15}$$

In practice, rather the eigenvalues of the inverse matrix are plot-

Fig. 7 Dispersion curves used to obtain the elastic moduli in the limit $|\mathbf{Q}| \to 0$, here for $L = 100$. The dotted lines indicate values from a different numerical method working at $|\mathbf{Q}| = 0$.

ted, see Fig. 7. The long-wavelength limit is then done by extrapolation by eye. The upper curve corresponds to the longitudinal waves, converging to $A_{xxxx} = (\mu - P) + (\lambda + \mu)$ in the limit $|\mathbf{Q}| \to 0$. The lower curve gives the transverse value $A_{xyxy} = \mu - P$.

The same limit can be done using the matrix D instead of G. The block structure helps to invert the large matrix, the inverse is again block-diagonal. The $d \times d$ blocks are simply the Fourier transforms of the matrices $D_{\alpha\beta}(\mathbf{n})$: $[\tilde{G}(\mathbf{m})^{-1}]_{\alpha\beta} = \tilde{D}_{\alpha\beta}(\mathbf{m})/N^2$. For the long-wavelength limit we expand the exponential in the definition of the Fourier transformation (13) around $\mathbf{Q_m} = 0$. The sum over the constant term vanishes, $\sum_{\mathbf{n}} D_{\alpha\beta}(\mathbf{n}) = 0$. The linear term vanishes due to symmetry, such that we obtain the quadratic term as the leading one. This conveniently matches with what we require for the limit in Eq. (15). Factorising the unit reciprocal vectors, we obtain for the elastic tensor

$$A_{\alpha\sigma\beta\tau} = -\frac{1}{2}\frac{kTN}{V_0}\sum_{\mathbf{n}} R_{\mathbf{n}\sigma}R_{\mathbf{n}\tau}D_{\alpha\beta}(\mathbf{n}). \qquad (16)$$

To determine the Lamé coefficients, we can either choose individual components such as A_{xxxx} above, or we can do a "hexagonal average", which amounts to reducing the rank-4 tensor to scalars, for example with $\delta_{\alpha\beta}\delta_{\sigma\tau}$ and with $\delta_{\alpha\sigma}\delta_{\beta\tau}$. This gives a 2×2 system of equations for $(\mu - P)$ and $(\lambda + \mu)$, which when solved becomes

$$\mu - P = -\frac{1}{16}\frac{kTN}{V_0}\sum_{\mathbf{n}} R_{\mathbf{n}}^2\big(3D_{\perp}(\mathbf{n}) + D_{\parallel}(\mathbf{n})\big) \qquad (17)$$

$$\lambda + \mu = \frac{1}{8}\frac{kTN}{V_0}\sum_{\mathbf{n}} R_{\mathbf{n}}^2\big(D_{\perp}(\mathbf{n}) - D_{\parallel}(\mathbf{n})\big) \qquad (18)$$

The summands are displayed in Fig. 8. They decrease with increasing distance, as expected, and their sums converge. We visualise the convergence in Fig. 9 where we added up the summands layer by layer. The final values are $\mu - P = 373$ and $\lambda + \mu = 553$.

In order to extract the Lamé coefficients, we need also the value of the pressure P. During simulations, we tracked the average flux of linear momentum, which is a mechanical definition of the pressure tensor. We further measured the response of this tensor to small deformations of the simulation box, which presents another (faster converging) way to calculate the elastic moduli. Notice
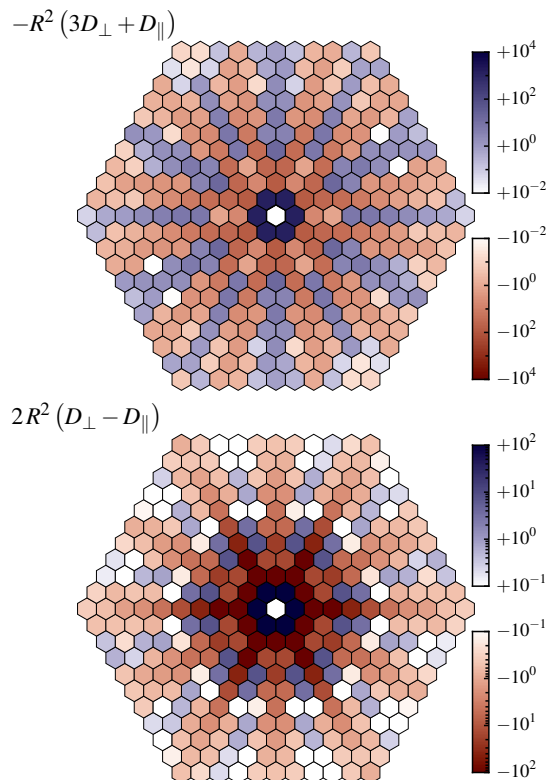
Fig. 8 The summands of Eqs. (17) and (18).
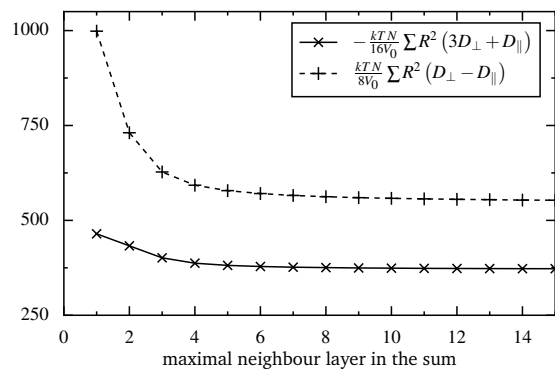
Fig. 9 Convergence of the sums in Eqs. (17) and (18).

that this method corresponds directly to "$|\mathbf{Q}| = 0$", no limit has to be taken. We obtain the values [*]

$$P = 34.4, \quad \mu = 405, \quad \lambda = 143.5. \qquad (19)$$

They are used in Fig. 7 to check the consistency of the different methods. Also the values extracted from Eqs. (17) and (18) are reasonably close.

2.3 Three-dimensional crystal

We also performed simulations in three dimensions, collecting high statistics data on a system of dimensions $L = 15$. Here, the result is similar to two dimensions, the effective interaction does not vanish beyond the layer of nearest neighbours but shows a rapid decrease. We adopt the same route of a rotated frame of reference to plot in Fig. 10 the matrix elements of the 3×3 matrices $D_{\alpha\beta}(\mathbf{n})$. We choose an orthonormal basis $(\hat{\mathbf{R}}_{\mathbf{n}}, \hat{\mathbf{o}}_1, \hat{\mathbf{o}}_2)$, in which the matrix comprises the following blocks:

$$\begin{pmatrix} D_\parallel & \mathbf{v}^T \\ \mathbf{w} & D_\perp \end{pmatrix} \qquad (20)$$

As before, $D_\parallel = \hat{\mathbf{R}}_{\mathbf{n}}^T D \hat{\mathbf{R}}_{\mathbf{n}}$, but $D_\perp$ is a 2×2 matrix, and $\mathbf{v}, \mathbf{w}$ are two-dimensional vectors. As the basis vectors $\hat{\mathbf{o}}_1, \hat{\mathbf{o}}_2$ can be chosen with an arbitrary rotation about the vector $\hat{\mathbf{R}}_{\mathbf{n}}$, we are only interested in invariants of $D_\perp, \mathbf{v}, \mathbf{w}$ under this rotation. For the matrix $D_\perp$ we thus plot in Fig. 10 the trace of $D_\perp$, its anti-symmetrised off-diagonals $D_{\perp,\mathrm{asym}}$ and some notion of its determinant. For $\mathbf{v}, \mathbf{w}$ we plot the modulus after (anti-)symmetrising, $D_{v,\mathrm{sym}} := \|\mathbf{v} + \mathbf{w}\|/2$, $D_{v,\mathrm{asym}} := \|\mathbf{v} - \mathbf{w}\|/2$. The lowest panel in Fig. 10 allows one to estimate the noise level for the given statistics.

If again one insists on an algebraic fit $D(\mathbf{n}) \propto \|\mathbf{R}/d_0\|^\alpha$, one finds $\alpha \approx -8 \pm 1$. In three dimension the data display less scatter when plotted in terms of neighbor layer, rather than separation. This is a nontrivial geometrical effect which is already visible in two dimensions: In the first panel of Fig. 5, the values on the diagonals of the hexagon are larger than the values at the same distance (even larger than those on the same neighbour level). This creates within every neighbour level (or distance) a tendency which is *opposed* to the general trend.

3 Effective interactions and the central force model

The simplest (Cauchy) model of elasticity in the physics of solids supposes that interactions are pairwise and central between all particles in the solid, deriving from a scalar potential. In this section we study the elastic properties of such systems, in order to better see where the numerical data demonstrates the presence
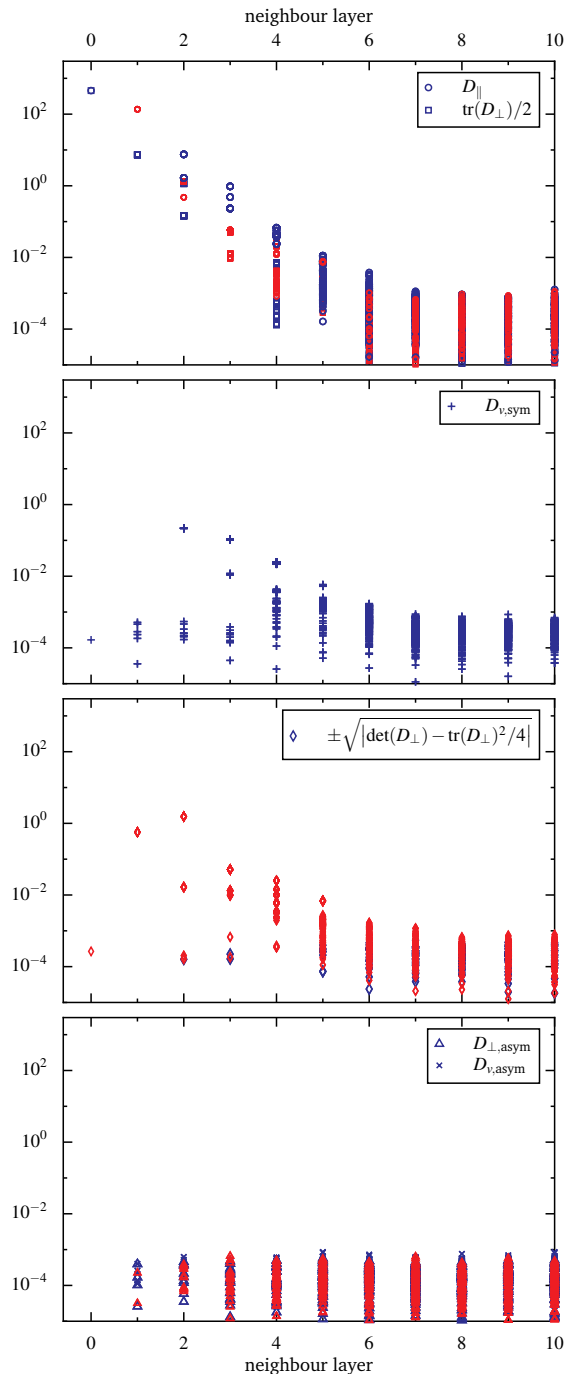
Fig. 10 Effective interactions in a FCC crystal of $N = 15^3$ hard spheres. Larger blue symbols are positive values, smaller red symbols are negative values. $K \sim 6.8 \times 10^4\, 3N$ recordings; volume fraction $\phi = 0.57$.

---

[*] These values are compatible with those given in Ref. 17. We applied the box-deformation method also to the value $\phi = 0.863714$ which is given in that reference, and our implementation reproduces exactly the given values for the elastic moduli. Concerning the numerical values of elastic moduli, there was a disagreement in the literature between Ref. 14 and Ref. 17, see also subsequent publications. Given that we implemented both the fluctuation method and two deformation methods (in a second one the spheres are deformed instead of the box) which all give the same result, we think that we can resolve the debate in favour of Ref. 17.

of non-central potentials.

The total potential energy Φ of a configuration is a function of all particle positions $\mathbf{r_i}$. It is expressed as a sum of functions $g_{\mathbf{ij}}$,

$$\Phi(\{\mathbf{r}\}) = \sum_{(\mathbf{ij})} g_{\mathbf{ij}}\left((\mathbf{r_i} - \mathbf{r_j})^2/2\right) \tag{21}$$

The sum runs over all different pairs of particles. To simplify the algebra and avoid square roots in the calculations, the $g_{\mathbf{ij}}$ are functions of the distance squared. The functions should be identical for symmetry-related pairs of particles, but otherwise each function is independent.

3.1 Description in terms of global deformations

The elastic behaviour of such a solid can be calculated via means of the canonical partition function and via a Taylor expansion of the Free Energy $F(\eta) = -kT \ln(Z(\eta))$ about zero strain ($\eta = 0$).[15] Here, the whole box is changed parametrically, with η being the parameter. We could therefore speak of a "$|\mathbf{Q}| = 0$" method which requires no long-wavelength limit. The resulting stress tensor and elastic tensor are expressed by the usual Gibbs-weighted average over configurations,[15]

$$T_{\alpha\beta} = \frac{1}{V_0} \frac{\partial F}{\partial \eta_{\alpha\beta}}(0)$$

$$= -kT \frac{N}{V_0} \delta_{\alpha\beta} + \frac{1}{V_0} \left\langle \sum_{(\mathbf{ij})} g'_{\mathbf{ij}} r_{\mathbf{ij},\alpha} r_{\mathbf{ij},\beta} \right\rangle \tag{22}$$

$$C_{\alpha\beta\sigma\tau} = \frac{1}{V_0} \frac{\partial^2 F}{\partial \eta_{\alpha\beta} \partial \eta_{\sigma\tau}}(0) = -2kT \frac{N}{V_0} \delta_{\alpha\tau} \delta_{\beta\sigma}$$

$$- \frac{1}{V_0 kT} \mathrm{Ccc}\left(\sum_{(\mathbf{ij})} g'_{\mathbf{ij}} r_{\mathbf{ij},\alpha} r_{\mathbf{ij},\beta}, \sum_{(\mathbf{ij})} g'_{\mathbf{ij}} r_{\mathbf{ij},\sigma} r_{\mathbf{ij},\tau} \right)$$

$$+ \frac{1}{V_0} \left\langle \sum_{(\mathbf{ij})} g''_{\mathbf{ij}} r_{\mathbf{ij},\alpha} r_{\mathbf{ij},\beta} r_{\mathbf{ij},\sigma} r_{\mathbf{ij},\tau} \right\rangle \tag{23}$$

Here, V_0 is the volume of the periodic box, and the sums run over all different pairs of particles, their difference vectors being denoted by $\mathbf{r_{ij}} := \mathbf{r_i} - \mathbf{r_j}$. The function $\mathrm{Ccc}(a,b) := \langle ab \rangle - \langle a \rangle \langle b \rangle$ is a cumulant-like cross-correlation function. The terms on the right-hand side of Eq. (22) are called the *kinetic* and the *virial* terms. The terms in Eq. (23) are called the *kinetic*, the *fluctuation*, and the *Born* terms.[15]

The virial term and the Born term relate a global change of strain, which is a *parametrical* change, to displacements of *individual* particles.

3.2 Description in terms of local displacements

Instead of global deformations, we would like to learn more about the energy of local deformations. For this we express the change of potential energy $\Phi(\{\mathbf{r}\})$ in terms of small-amplitude displacements around the reference state (positions $\mathbf{R_i}$ on the Bravais lattice). The reference state is perfectly hexagonal and thus has inversion symmetry, which imposes that the partial first derivatives

vanish when evaluated at the reference positions:

$$\frac{\partial \Phi}{\partial r_{\mathbf{i}\alpha}}(\{\mathbf{R}\}) = 0 \tag{24}$$

for all $\mathbf{i}$ and α.[†] From Eq. (24) it follows that the increase in potential energy of the system due to local displacements is given to quadratic order by

$$\Delta\Phi := \Phi(\{\mathbf{r}\}) - \Phi(\{\mathbf{R}\}) = \frac{1}{2} \sum_{\alpha,\beta,\mathbf{i},\mathbf{j}} H_{\alpha\beta}(\mathbf{j}-\mathbf{i}) u_{\mathbf{i}\alpha} u_{\mathbf{j}\beta} \tag{25}$$

where, as above, $\mathbf{u_i} = \mathbf{r_i} - \mathbf{R_i}$ is the displacement vector of particle $\mathbf{i}$. The idea of this section is to assume that the configurations are normal distributed with weights $\exp\{-\Delta\Phi/kT\}$. The inverse of the displacement correlation is then given by the Hessian matrix, $\langle u_{\mathbf{i}\alpha} u_{\mathbf{j}\beta} \rangle^{-1} = H_{\alpha\beta}(\mathbf{j}-\mathbf{i})/kT$. It is easier to understand the true interactions after studying this simplified problem, and it is thus worth while comparing H and D. We remember that the units here are chosen such that $kT = 1$. The Hessian matrix consists of second derivatives, evaluated at the reference positions,

$$H_{\alpha\beta}(\mathbf{j}-\mathbf{i}) := \frac{\partial^2 \Phi}{\partial r_{\mathbf{i}\alpha} \partial r_{\mathbf{j}\beta}}(\{\mathbf{R}\}). \tag{26}$$

Start with the first derivative

$$\frac{\partial \Phi}{\partial x_{\mathbf{i}}}(\{\mathbf{r}\}) = \sum_{\mathbf{j} \neq \mathbf{i}} (x_{\mathbf{i}} - x_{\mathbf{j}}) g'_{\mathbf{ij}} \tag{27}$$

and obtain $H_{\alpha\beta}(\mathbf{j}-\mathbf{i})$ for $\mathbf{i} \neq \mathbf{j}$:

$$H_{\alpha\beta}(\mathbf{j}-\mathbf{i}) = -(R_{\mathbf{i}\alpha} - R_{\mathbf{j}\alpha})(R_{\mathbf{i}\beta} - R_{\mathbf{j}\beta}) g''_{\mathbf{ij}} - \delta_{\alpha\beta} g'_{\mathbf{ij}}, \tag{28}$$

We abbreviate our notation by introducing $\mathbf{R_{j-i}} = \mathbf{R_j} - \mathbf{R_i}$ and $g_{\mathbf{j-i}} = g_{\mathbf{ij}}$ and obtain

$$H_{\alpha\beta}(\mathbf{n}) = -R_{\mathbf{n}\alpha} R_{\mathbf{n}\beta} g''_{\mathbf{n}} - \delta_{\alpha\beta} g'_{\mathbf{n}}. \tag{29}$$

At $\mathbf{j} = \mathbf{i}$, the matrix is constrained by the fact that the sum over all $\mathbf{n}$ vanishes,

$$H_{\alpha\beta}(\mathbf{0}) = -\sum_{\mathbf{n} \neq \mathbf{0}} H_{\alpha\beta}(\mathbf{n}). \tag{30}$$

We can compare $H_{\alpha\beta}(\mathbf{n})$ and $D_{\alpha\beta}(\mathbf{n})$ in different frames of reference. In the rotated frame in which one axis is aligned with the difference vector, we find

$$H_{\|}(\mathbf{n}) = -\mathbf{R_n^2} g''_{\mathbf{n}}(\mathbf{R_n^2}/2) - g'_{\mathbf{n}}(\mathbf{R_n^2}/2)$$

$$H_{\perp}(\mathbf{n}) = -g'_{\mathbf{n}}(\mathbf{R_n^2}/2) \tag{31}$$

$$H_{\mathrm{sym}}(\mathbf{n}) = 0.$$

The corresponding results for the hard sphere system are plotted in Fig. 5. It is striking that $H_{\mathrm{sym}}(\mathbf{n})$ is zero for all $\mathbf{n}$, whereas $D_{\mathrm{sym}}(\mathbf{n})$ has nonzero values, which must be a consequence of

---

[†] Notice that we do not globally deform the system when displacing individual particles. The vanishing of the first derivatives in Eq. (24) thus does not contradict the nonzero pressure in the reference state, but we cannot calculate it from Eq. (24)
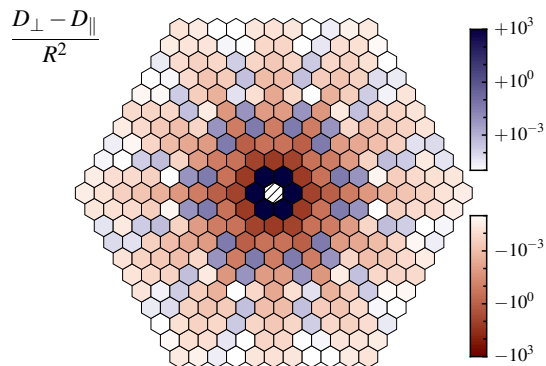
$$\frac{D_\perp - D_\parallel}{R^2}$$

Fig. 11 The combination of matrix elements $D(\mathbf{n})$ used in Eq. (32).

non-central forces in the effective theory. We note that $D_{\text{sym}}(\mathbf{n})$ is smaller in amplitude than $D_\parallel$ and $D_\perp$, so that the non-central nature can be considered as a correction to the dominant terms. We also see that $g'_{\mathbf{n}}$ can be read off from the perpendicular component, which allows to calculate the effective force between particles, being $\mathbf{f}(\mathbf{n}) = \pm \mathbf{R}_{\mathbf{n}} g'_{\mathbf{n}}$. We can also extract the second derivative

$$g''_{\mathbf{n}}(\mathbf{R}_{\mathbf{n}}^2/2) = \frac{H_\perp(\mathbf{n}) - H_\parallel(\mathbf{n})}{\mathbf{R}_{\mathbf{n}}^2}. \tag{32}$$

Figure 11 shows the corresponding values for the matrices D.

We can also examine the results in the non-rotated frame, for which the corresponding values of D were given in Fig. 6. In particular, for the off-diagonal terms we find

$$H_{xy}(\mathbf{n}) = -X_{\mathbf{n}} Y_{\mathbf{n}} g'_{\mathbf{n}}. \tag{33}$$

We find the same antisymmetry with respect to the x-axis and the y-axis that was observed in Fig. 6.

3.3 Continuum limit

We can do the same long-wavelength limit that led to Eq. (16) also with the matrix $H(\mathbf{n})$ instead of $D(\mathbf{n})$. This will lead us back to the global tensors of Sec. 3.1. Starting with the discrete Fourier transform, then expanding the exponential and eliminating the sum according to Eq. (30) yields the equivalent of Eq. (16),

$$\bar{A}_{\alpha\sigma\beta\tau} := -\frac{N}{2V_0} \sum_{\mathbf{n}} R_{\mathbf{n},\sigma} R_{\mathbf{n},\tau} H_{\alpha\beta}(\mathbf{n})$$

$$= \frac{N}{2V_0} \sum_{\mathbf{n}} R_{\mathbf{n},\sigma} R_{\mathbf{n},\tau} \left(R_{\mathbf{n},\alpha} R_{\mathbf{n},\beta} \, g''_{\mathbf{n}} + \delta_{\alpha\beta} \, g'_{\mathbf{n}} \right). \tag{34}$$

We use an overbar to distinguish this tensor from the true elastic tensor. The corresponding Lamé coefficients $\bar{\lambda}, \bar{\mu}$ can be obtained from $\bar{A}$ as in Eq. (8), if the effective stress tensor is known. We note that the effective force between two particles is given by

$$\mathbf{f}_{\mathbf{ij}} = -(\mathbf{R}_{\mathbf{i}} - \mathbf{R}_{\mathbf{j}}) g'_{\mathbf{ij}}. \tag{35}$$

The virial part of the stress tensor is thus

$$\bar{T}_{\sigma\tau} = -\frac{1}{2V_0} \sum_{(\mathbf{ij})} (\mathbf{R}_{\mathbf{i}} - \mathbf{R}_{\mathbf{j}})_\sigma f_{\mathbf{ij},\tau}$$

$$= \frac{N}{2V_0} \sum_{\mathbf{n}} R_{\mathbf{n},\sigma} R_{\mathbf{n},\tau} g'_{\mathbf{n}}. \tag{36}$$

This sum was already found as the last term of Eq. (34). According to the relation between the elastic tensors $\bar{A}$ and $\bar{C}$, Eq. (8), $\bar{C}$ is of appealingly simple form,

$$\bar{C}_{\alpha\sigma\beta\tau} = \frac{N}{2V_0} \sum_{\mathbf{n}} R_{\mathbf{n},\alpha} R_{\mathbf{n},\sigma} R_{\mathbf{n},\beta} R_{\mathbf{n},\tau} g''_{\mathbf{n}}. \tag{37}$$

Both sums in Eq. (36) in Eq. (37) occurred in very similar form in the virial part of the stress tensor, Eq. (22), and in the Born term of the elastic tensor, Eq. (23). This is of course no coincidence. Both kinetic terms and the fluctuation term are missing, however. The absence of these terms implies that the tensor $\bar{C}$ has a higher symmetry than the true elastic tensor in Eq. (6). It is invariant under arbitrary index permutations and therefore satisfies the Cauchy relation $\bar{\mu} = \bar{\lambda}$.

In the same way as we calculated the Lamé coefficients from D, we can proceed here. The result is already given by Eq. (18) because of the Cauchy relation. In terms of the functions $g_{\mathbf{n}}$ it reads

$$\bar{\lambda} = \bar{\mu} = \frac{N}{16V_0} \sum_{\mathbf{n}} R_{\mathbf{n}}^4 g''_{\mathbf{n}}. \tag{38}$$

The values for μ and λ in Eqs. (19) show that the hard-disk crystal is far from being Cauchy. If we blindly apply Eq. (38) to the data, using $R^2(D_\perp - D_\parallel)$ as the summand, according to Eq. (32), then we simply calculate the average value $(\mu + \lambda)/2$. This might sound quite acceptable to some. How conceptually wrong this procedure is can be exemplified for the pressure: It is minus a diagonal term of the stress in Eq. (36), or $\bar{P} = -\frac{N}{4V_0} \sum_{\mathbf{n}} R_{\mathbf{n}}^2 g'_{\mathbf{n}}$. If we take $-D_\perp(\mathbf{n})$ for $g'_{\mathbf{n}}$, motivated by Eq. (31), then we find the value -96 for this effective pressure. This is clearly unacceptable – even the sign is wrong. In fact, a close look on Eqs. (17) and (18) reveals that the sum calculates actually $P + (\lambda - \mu)/2$ and equals the pressure only to the extent that the Cauchy relations are satisfied.

One concludes that the central force model is too simplified for detailed modeling of the elastic properties of hard spheres. However, in softer systems one might hope that such an analysis remains useful.

4 Conclusions

We have collected very high statistics data on the effective interactions generated in a hard-sphere system. In one dimension the results are trivial, as was expected: The effective interactions between hard rods are limited to nearest neighbours. In higher dimensions (two and three) the results are much more interesting. Despite the true interactions being localized to nearest neighbours, we find farther-reaching effective interactions from the analysis of displacement correlations.

The theoretical interpretation of these results seems difficult. We provide a first interpretation in Section 3 in terms of the

Cauchy model, which uses pairwise central interactions. Interestingly, when analysed in terms of global strains, this model does not imply the Cauchy relation (Sec. 3.1) but allows the full set of Lamé coefficients – as required by the numerical realization. The calculation cannot yield, however, information on the range and decay of the effective interactions. These interactions are accessible in the setting of Sec. 3.2 where individual particles are displaced. Unfortunately this setting does not reproduce correctly the global symmetry of the elastic moduli but rather predicts that $\lambda = \mu$ (Cauchy relation). It further predicts that some elements of D are strictly zero, for for instance D_{sym} – This is clearly not realized by the numerical system.

The presented results thus open the quest for a better calculation than the one in Sec. 3.2. In particular one would like to predict how the effective interactions decay with distance. One possibility might be to start with a weakly perturbed Gaussian system and add extra non-linearities and non-central forces as perturbations. But this is rather *ad hoc*, and it is not clear exactly what should be the set of extra terms that could be added.

References

1 P. J. Yunker, K. Chen, M. D. Gratale, M. A. Lohr, T. Still and A. G. Yodh, *Reports on Progress in Physics*, 2014, **77**, 056601.

2 S. M. Underwood, J. R. Taylor and W. van Megen, *Langmuir*, 1994, **10**, 3550–3554.

3 C. Brito, O. Dauchot, G. Biroli and J.-P. Bouchaud, *Soft Matter*, 2010, **6**, 3013–3022.

4 S. Henkes, C. Brito and O. Dauchot, *Soft Matter*, 2012, **8**, 6092–6109.

5 A. Ghosh, R. Mari, V. Chikkadi, P. Schall, A. Maggs and D. Bonn, *Physica A: Statistical Mechanics and its Applications*, 2011, **390**, 3061 – 3068.

6 K. Chen, W. G. Ellenbroek, Z. Zhang, D. T. N. Chen, P. J. Yunker, S. Henkes, C. Brito, O. Dauchot, W. van Saarloos, A. J. Liu and A. G. Yodh, *Phys. Rev. Lett.*, 2010, **105**, 025501.

7 A. Ghosh, V. K. Chikkadi, P. Schall, J. Kurchan and D. Bonn, *Phys. Rev. Lett.*, 2010, **104**, 248305.

8 C. A. Lemarchand, A. C. Maggs and M. Schindler, *EPL (Europhysics Letters)*, 2012, **97**, 48007.

9 K. Chen, T. Still, S. Schoenholz, K. B. Aptowicz, M. Schindler, A. C. Maggs, A. J. Liu and A. G. Yodh, *Phys. Rev. E*, 2013, **88**, 022315.

10 M. Born and K. Huang, *Dynamical Theory of Crystal Lattices*, Oxford University Press, Oxford, 1998.

11 S. Pronk and D. Frenkel, *Phys. Rev. Lett.*, 2003, **90**, 255501.

12 D. Frenkel and A. J. C. Ladd, *Phys. Rev. Lett.*, 1987, **59**, 1169–1169.

13 D. C. Wallace, in *Thermoelastic Theory of Stressed Crystals and Higher-Order Elastic Constants*, ed. H. Ehrenreich, F. Seitz and D. Turnbull, Academic Press, New York and London, 1970, vol. 25, pp. 301–404.

14 S. Sengupta, P. Nielaba, M. Rao and K. Binder, *Phys. Rev. E,* 2000, **61**, 1072–1080.

15 D. Squire, A. Holt and W. Hoover, *Physica*, 1969, **42**, 388 – 397.

16 C. D. Barnes and D. A. Kofke, *The Journal of Chemical Physics*, 1999, **110**, 11390–11398.

17 K. W. Wojciechowski, K. V. Tretiakov, A. C. Brańka and M. Kowalik, *The Journal of Chemical Physics*, 2003, **119**, 939–946.